New insights in the morphological characterization and modelling of poly(-caprolactone) bone scaffolds obtained by supercritical CO2 foaming

(Article begins on next page)

New insights in the morphological characterization and modelling of poly(ε-caprolactone) bone scaffolds obtained by supercritical CO$_2$ foaming

Víctor Santos-Rosales [a,*], Marta Gallo [b,c], Philip Jaeger [d], Carmen Alvarez-Lorenzo [a], José L. Gómez-Amoza [a], Carlos A. García-González [a,*]

[a] Dept. Farmacología, Farmacia y Tecnología Farmacéutica, I+D Farma Group (GI-1645), Faculty of Pharmacy, Agrupación Estratégica de Materiales (AeMAT), and Health Research Institute of Santiago de Compostela (IDIS), Universidade de Santiago de Compostela, E-15782, Santiago de Compostela, Spain
[b] Department of Applied Science and Technology, Politecnico di Torino, Corso Duca degli Abruzzi 24, 10129, Torino, Italy
[c] University of Lyon, INSA de Lyon, MATEIS UMR CNRS 5510, Bât. Saint Exupery, 23 Av. Jean Capelle, F-69621, Villeurbanne, France
[d] Hamburg University of Technology (TUHH), Eißendorfer Str. 38, D-21073, Hamburg, Germany

HIGHLIGHTS

- Process-structure-functionality relationships of manufactured scaffolds were elucidated.
- The combined μ-CT/MIP analysis allowed a full morphological characterization of scaffolds.
- CO$_2$ soaking time had a dramatical effect on the scaffold architectures
- 3D models of the porous structure were obtained for the manufactured scaffolds.
- Scaffolds were screened from in silico cell infiltration and water permeability tests.

GRAPHICAL ABSTRACT
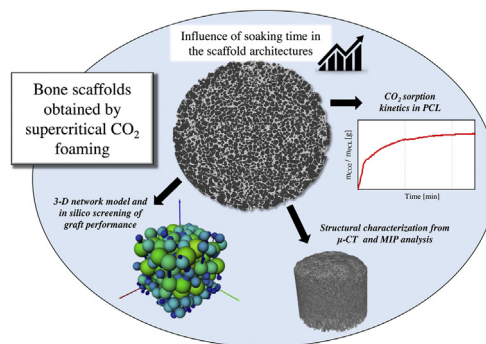
ARTICLE INFO

ABSTRACT

Hierarchically porous synthetic bone grafts (scaffolds) are gaining attention in the clinical arena. Scaffolds should combine morphological (macro- and microporosity, pore interconnectivity), mechanical and biological (biocompatibility, degradation rate) properties to fit this specific use. Supercritical (sc-) foaming is a versatile scaffold processing technology. However, the selection of the optimum operating conditions to obtain a defined scaffold structure is hampered by the lack of a single characterization technique able to fully elucidate the porous features of the resulting scaffolds. In this work, the effect of soaking time (1, 3 and 5 h) on the preparation of poly(ε-caprolactone) (PCL, 50 kDa) scaffolds by sc-foaming was evaluated by a combined X-ray microtomography (μ-CT) and mercury intrusion porosimetry (MIP) 3D-morphological analysis. Mechanical tests and in silico modelling for cell penetration and water permeability of the scaffolds were also conducted. Results evidenced the relevance of μ-CT and MIP as a synergistic analytical duo to fully elucidate the morphology of the sc-foamed scaffolds and the soaking time effect.

* Corresponding authors.
E-mail addresses: victor.santos.rosales@rai.usc.es (V. Santos-Rosales), carlos.garcia@usc.es (C.A. García-González).

1. Introduction

Bone is the second most common transplantation tissue and the harvesting of cancellous bone from the patient (allografts) is the current gold-standard surgical procedure to repair bone defects in the locomotor system. Nevertheless, the risk of infections, the intervention-associated damages and the limited availability of transplantable tissue evidence the need of new therapeutic approaches. The development of innovative synthetic grafts, the so-called scaffolds, provides a promising strategy to regenerate damaged tissues promoting the self-healing capacity of the patients. Scaffolds must display a 3D-interconnected and hierarchical porous structure and a mechanical behavior that are adapted to the anatomical target to get an appropriate performance once implanted [1].

Conventional methods for scaffold manufacturing frequently involve the use of high temperatures and/or organic solvents and may require long and tedious downstream pathways [2–4]. These processing conditions are usually incompatible with scaffolds containing bioactive compounds (*i.e.* medicated scaffolds) which do not withstand harsh treatments and may be also lost during purification. The use of medicated scaffolds is of particular interest to improve the scaffold integration and the precise tissue regeneration or to alleviate post-surgical harms. Supercritical (sc-) foaming is a versatile solvent-free green technology for the processing of biodegradable polymeric scaffolds. Sc-foaming is based on the sorption and dissolution of CO_2 in the polymeric matrix of the scaffold for a certain time period (soaking time; ST) under certain pressure (batch pressure; BP) and temperature (batch temperature; BT), followed by a pressure release (depressurization rate; DR). The latter step forces the polymer expansion and CO_2 removal in order to induce the formation of pores in the polymeric matrix. Due to the plasticizing effect of CO_2, sc-foaming technology operates under moderate processing temperatures, *i.e.* compatible with the incorporation of thermolabile bioactive compounds such as growth factors [5–7], anti-inflammatory drugs [8–10] or antimicrobial agents [11–13] of interest for bone regeneration.

The fine control of the main operating variables of sc-foaming (BP, BT, ST, DR) allowed the manufacturing of tunable porous and interconnected architectures for polyester-based scaffolds, such as poly(D,L-lactic acid) (PLA) [14], poly(lactic-*co*-glycolic acid) (PLGA) [15,16], poly(ε-caprolactone) (PCL) [17,18] or poly(L-lactide-co-ε-caprolactone) (PLCL) [19]. Rational design of patient-personalized and quality-reproducible scaffolds demands the development of standard operating procedures (SOP) for sc-foaming. Compilation of protocols and processing parameters is of utmost importance to obtain scaffolds fitted to the target grafting site demands, particularly in terms of pore size, morphology, distribution, throat size and interconnection that are critical for cell colonization and differentiation [20]. However, the modelling of the pore formation mechanism during sc-foaming process is still challenging but absolutely required for the definition of SOPs.

There are few studies reporting on the effects of the foaming processing conditions on the resulting polymeric scaffold 3D-architectures [18,21–24]. Commonly, morphological characterization is carried out by scanning electron microscopy (SEM), which allows for direct measurements of pore sizes and visual estimations of pore interconnectivity although restricted to the exposed surface area. The evaluation of scaffolds using the SEM approach has severe limitations mainly related to the sample preparation itself and the method of data treatment. A physical sectioning of the scaffold is required as a previous step to expose the inner regions. This preparative step is usually performed manually using a surgical blade that makes the sample to be under compression and shear forces. These forces may cause structural damages to the structure, such as pore occlusion and deformation [25]. Moreover, flawed cuts of the scaffolds are frequent depending on the dimensions and the difficulty of handling of the scaffold; the obtained angled areas also compromise the quality and reliability of the results. Finally, the data treatment of SEM images to study the pore size distribution considers the size of a pore equivalent to the cross-section diameter of the pore in the SEM-image. This assumption usually results in an underestimation of the actual pore sizes in the case of spherical pores. For the case of elongated (cylindrical) pores, several specimens cut in the axial and coronal plane are needed to get a reliable pore size distribution from SEM images, requiring more amount of material as they are destructive tests.

Mercury intrusion porosimetry (MIP) is a well-established technique for the characterization of porous materials, based on the profile of mercury intrusion into pores when subjected to increasing pressures. Once the maximum pressure is reached, an extrusion profile is also obtained from the depressurization step. From both profiles, the pore and throat sizes of the sample can be calculated, and the pore tortuosity, compressibility or permeability may be inferred [26,27]. Despite the advantages of the technique, MIP is not a suitable characterization method for materials with large macropores due to its upper-limit measurable pore range (up to *ca.* 200 μm) [28]. In addition, MIP does not take into account close pores and assumes perfectly cylindrical pores to correlate the volume of mercury intruded with the pore size, which do not always represent the reality of the analyzed samples [25,29].

X-ray-based microtomography (μ-CT) is a non-invasive method that provides quantitative and qualitative information regarding the 3D-morphology of samples and is commonly used for the analysis of trabecular bone [30,31]. The use of this technique is encouraging for scaffold characterization [32–37], although there are two main aspects to consider when performing a μ-CT scan: the duration of the analysis and the storage of the obtained data. Indeed, the scanning of low volume samples can last over 20 h and the generated files have sizes in the order of several terabytes depending on the μ-CT acquisition parameters (*e.g.* voxel size, rotation step) [38]. Also, the selected voxel size has a direct impact on the image resolution from the μ-CT scan and, subsequently, on the lowest value of measurable pore size of the porous materials. Therefore, a trade-off solution between the image resolution and the time-cost and data storage space consumption must be met.

Overall, the state-of-the-art of morphological characterization of scaffolds indicates that there is not a universal technique able to fully characterize the porous structure of polymeric scaffolds in the micro-to-macroporous range regarding pore-throat distributions and pore interconnectivities.

The combination of these complementary techniques (SEM, MIP and μ-CT) for the full characterization of scaffold pore structure can overcome the individual artifacts or pitfalls of each individual technique. To the best of our knowledge, it is the first time that the combination of these characterization techniques is exploited to generate information on process-structure-functionality relationships of scaffolds obtained by sc-foaming, which is of utmost interest for the definition of SOPs. Thus, the effect of the CO_2 soaking time during the supercritical foaming process on the scaffold morphology was evaluated to get the target scaffold features required for synthetic bone grafts. The morphological study of the resulting scaffolds of poly(ε-caprolactone) (PCL), a bioresorbable semicrystalline polymer [39–45], was performed based on the combination of SEM, MIP, helium pycnometry and μ-CT techniques. *In silico* studies of cell infiltration capacity and water permeability as well as *in vitro* mechanical tests were carried out for the sc-foamed scaffolds to predict the graft performance once implanted.

2. Materials and methods

2.1. Materials

Poly(ε-caprolactone) (PCL) in the powdered form (50 kDa, T_m = 61.4 °C, 66.7 % crystallinity) was supplied by Polysciences (Warrington, PA, USA). CO_2 (purity >99.9 %) was employed as foaming and blowing agent and provided by Praxair, Inc. (Madrid, Spain).

2.2. CO_2 sorption kinetics

A thermostized magnetic suspension balance (Rubotherm GmbH, Bochum, Germany) was used to evaluate the CO_2 sorption kinetics on the PCL at 140 bar and 39 °C, *i.e.* conditions close to body temperature and where PCL was molten according to preliminary view cell tests (not shown). The polymeric powder was dosed (80 mg) in a glass container and attached to the balance through a metal hook. Prior to the measurements, the polymer was molten at 80 °C in an oven to ensure a homogeneous CO_2 sorption along the material [46].

2.3. Processing of PCL scaffolds by sc-foaming

PCL powder was weighed (*ca.* 1 g) and dosed in cylindrical (length = 24.6 mm, internal diameter = 17 mm) Teflon moulds (Brand GmbH, Wertheim, Germany), followed by manual compression. Moulds were then placed in a 100 mL-stainless steel autoclave (Thar Process, Pittsburg, PA, USA) and heated to 39 °C (BT). Afterwards, the system was pressurized with CO_2 (5 g/min) until 140 bar (BP) and maintained in the static mode for a certain soaking period (ST = 1, 3 and 5 h). The system was stirred at 700 rpm during the whole process to enhance the mass transfer and to ensure a homogeneous CO_2 environment. The autoclave was then depressurized at a constant venting rate (DR = 1.8 g/min) until atmospheric pressure. Prior to their storage, the outer skin of the scaffolds was carefully removed using a surgical blade. Scaffolds were denoted as 39_{ST} referring to the processing temperature (BT= 39 ºC) and the subscript according to the soaking time used (ST= 1h, 3h or 5h).

2.4. Characterization of scaffolds

2.4.1. Structural characterization

Bulk densities (ρ_{bulk}) were obtained from the ratio between the weight and volume of each scaffold after sc-foaming. The skeletal density (ρ_{skel}) of the scaffolds was determined using a helium-pycnometer (Quantachrome, Boynton Beach, FL, USA) at room temperature (25 °C) and 1.01 bar. Values were obtained from six replicates. Overall porosity (ε) was calculated according to Eq. (1).

$$\varepsilon \ (\%) = \left(1 - \frac{\rho_{bulk}}{\rho_{skel}} \right) x \ 100 \tag{1}$$

The morphological properties of the scaffolds were investigated by scanning electron microscopy (FESEM, ULTRA PLUS, Zeiss, Oberkochen, Germany) running at a voltage of 10 kV. Prior to their imaging, scaffolds were sliced with a scalpel and then iridium-sputtered (10 nm thickness).

2.4.2. MIP analyses and *in silico modelling of PCL scaffolds*

MIP analyses of the PCL scaffolds were performed (Autopore IV 9500 model, Micromeritics, Norcross, GA, USA) at working pressures ranging from 0.07−1800 bar to determine their pore size distributions in the 0.01−180 μm range. Porosity values (ε_{MIP}) and pore size (*MIP-Mean pore size*) were determined from the intruded volume of mercury ($V_{p_{MIP}}$) in the scaffolds with the increase of pressure using the Washburn equation [25]. A 3D-network model was

generated from the MIP-cumulative curves having identical percolation properties as those of the manufactured PCL-scaffolds using PoreXpert v.1.6.567 software (PoreXpert Ltd, Plymouth, UK). This *in silico* model consists in a cubic structure formed by 1,000 pores (of cubic shape) connected by up to 3,000 throats of arbitrary cylindrical shape. A Boltzmann-annealed simplex algorithm was used to estimate and to simultaneously optimize the connectivity (mean number of throats per pore), pore skew, throat skew and correlation level from the MIP-cumulative curves. Water permeability (25 °C, 1.03 bar) was estimated assuming that Poiseuille flow (water) occurred in the z-direction according to Eq. (2)

$$k_w = \frac{\pi}{8} \omega_{cell} (Farcs) \frac{l_{cell}}{A_{cell}} \tag{2}$$

where l_{cell} and A_{cell} represent the length and the cross-sectional area of the unit cell, respectively, and ω_{cell} (Farcs) is an averaging operator over the whole unit cell operating on the flow capacities of the pore throat-pore arcs parallel to the z-axis. PoreXpert calculates the term ω_{cell} (Farcs) by means of the Dinic network analysis algorithm. Mesenchymal stem cells (MSCs) infiltration in the scaffolds was simulated using the filtration module from the software and assuming a cell size of 26.5 ± 5.0 μm, an average value for human MSCs [47–49].

2.4.3. Micro X-ray computed tomography image acquisition, reconstruction and analysis

Micro X-ray computed tomography (μ-CT) scans were acquired (in the local mode) using a Phoenix v|tome|x tomograph (GE, Boston, MA, USA) equipped with a Varian PaxScan detector (1920 × 1536 pixels). Voxel resolution was set equal to 12 μm.

3D images were reconstructed and analyzed using Avizo v.2019.1 software (Thermo Fisher Scientific, Waltham, MA, USA). A general scheme of the workflow from the image acquisition to complete 3D reconstruction and analysis is depicted in Fig. 1. Firstly, a specific region of interest (ROI) of cubic shape ($4.8 \times 4.8 \times 4.8 \ mm^3$) and representative of the entire scaffold was isolated to evaluate the influence of the working parameters on the resulting morphologies. Afterwards, the calibration of the thresholding of the grey-scale was performed to differentiate the void fraction (pores and pore interconnections, *i.e.* throats) from the solid material. This image thresholding is considered a crucial step prior to 3D modelling that influences the subsequent analysis and structural plots [50]. Once the void volume was precisely identified, porosity ($\varepsilon_{\mu\text{-CT}}$) of the scaffolds was calculated in the ROI and expressed as percentage of void voxels with respect to the total number of voxels. Connected porosity of the scaffolds was calculated (in percentage) as the volume fraction of the largest group of interconnected pores with respect to the total pore volume in the ROI of the material. Tortuosity was calculated from the mean pathway distance of a particle moving from one face of the ROI to the opposite one divided by the length of the edge of the cubic ROI (*i.e.* the shortest possible pathway).

A 3D-network model of balls and struts was also obtained from the μ-CT data, where the pores are represented as balls and the pore throats as cylindrical struts. The sizes of balls and struts were calibrated according to a color scale to visually identify morphological differences between scaffolds. In addition, pore size and pore throats distributions and their mean values were obtained based on the former 3D model. Finally, simulated MIP-data and pore volume distributions of the PCL-scaffolds were obtained from the 3D model generated from μ-CT using Xlib plugin from Fiji-ImageJ software [51,52].

2.4.4. Mechanical properties

PCL scaffolds (in triplicate) were subjected to unidirectional compression tests in a tensile bench with a 30 kg load cell
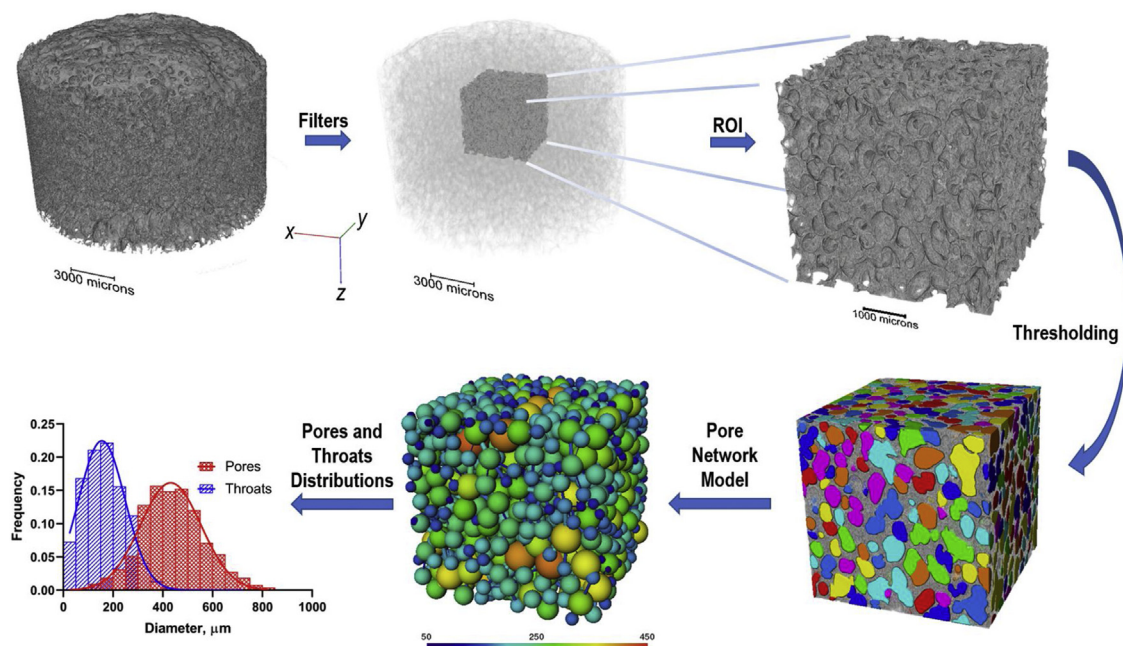
Fig. 1. Data processing pathway used for the micro X-ray computed tomography image acquisition, reconstruction and analysis of the supercritical CO_2 foamed scaffold. Firstly, a specific region is isolated from the entire scaffold. Through the image thresholding step, the void fraction is converted to a 3D-network model of balls and struts, whose sizes are calibrated according to a color scale, and the solid material in gray. Based on the 3D model, pore size and throats distribution plots are obtained.
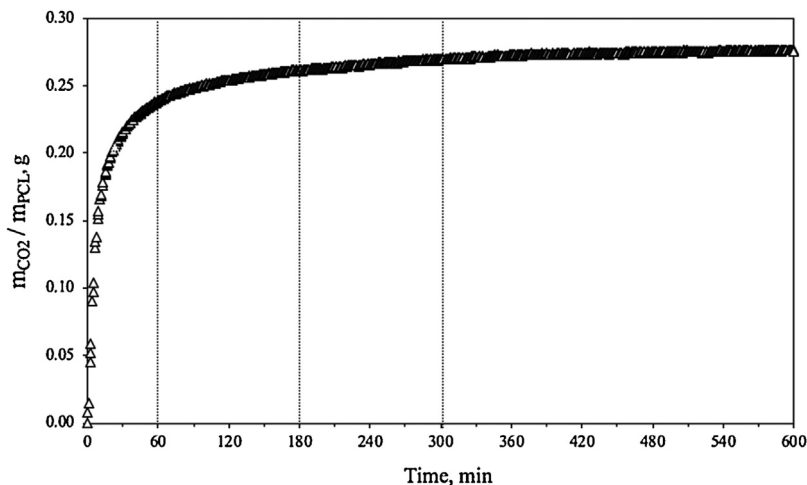
Fig. 2. CO_2 sorption kinetics in PCL at the sc-foaming conditions (140 bar and 39 °C). Parallel dotted lines indicate the three soaking times (60, 180 and 300 min) chosen to evaluate the influence of the amount of CO_2 absorbed on the resulting foam morphologies.

(TA.XT*Plus*, Stable Micro Systems, Ltd., Godalming, UK) at a crosshead speed of 1 mm/min. All the experiments were performed at room temperature (25 °C), atmospheric pressure and 45 % relative humidity. Elastic deformation was calculated from the ratio between the initial height and the height of the sample bearing the highest applied physical stress. The Youngś modulus (E) was calculated from the stress-strain plots previous conversion to engineering stress and engineering strain.

2.5. Statistical analysis

All results were expressed as mean ± standard deviation. Statistical analyses of the mechanical results (1-way ANOVA) were performed using Statistica v8.0 software (StatSoft Inc., Tulsa, OK, USA) followed by the post-hoc Tukey HSD multiple comparison test.

3. Results and discussion

3.1. Experimental CO_2 sorption kinetics in PCL

Solubility and diffusivity of CO_2 within a polymer can be modulated by tuning the working temperature and pressure leading to dramatic changes in the resulting foam morphologies [53]. The CO_2 sorption profile in PCL under an atmosphere of sc-CO_2 at 140 bar and 39 °C is shown in Fig. 2. The amount of CO_2 absorbed in PCL was greatly influenced by the soaking time with a fast CO_2 sorption kinetics followed by a slower stage after *ca.* 60 min of exposure with values in the near-saturation range (0.23−0.27 grams of CO_2 absorbed per gram of PCL). The solubility values of CO_2 at 35 °C and 130 bar, and 40 °C and 150 bar were previously reported to reach 0.22 and 0.40 g CO_2/g PCL at the saturation stage, respectively [17,54]. The broad range between these two values indicates the proximity of the phase transition and shows that the reported

Table 1
Morphological and textural properties of PCL scaffolds obtained by sc-foaming. Density values expressed as mean values ± standard deviation (n = 6).

Scaffold	ρ_{bulk}(g/cm^3)	ρ_{skel}(g/cm^3)	ε(%)	ε_{MIP}(%)	$V_{p_{MIP}}$(cm^3/g)	MIP-Mean pore size (μm)	$\varepsilon_{\mu-CT}$(%)	μ-CT-Mean pore size[a](μm)	μ-CT-Mean pore size[b](μm)
39$_{1h}$	0.353 ± 0.007	1.101 ± 0.013	68.0 ± 0.7	30.7	1.70	110.29	67.9	733.2 ± 466.5	1340 ± 341
39$_{3h}$	0.317 ± 0.019	1.110 ± 0.011	71.4 ± 1.7	13.1	1.99	116.23	67.2	733.6 ± 330.1	1096 ± 527
39$_{5h}$	0.298 ± 0.008	1.084 ± 0.009	72.5 ± 0.8	20.2	2.31	117.14	68.3	416.7 ± 123.1	698 ± 430

[a] Values obtained from the 3D-model reconstruction. Values follow a normal distribution (R^2> 0.99).

[b] Values obtained from the 2D-images of the μ-CT analysis in the axial plane. Values follow a normal distribution (R^2> 0.72).
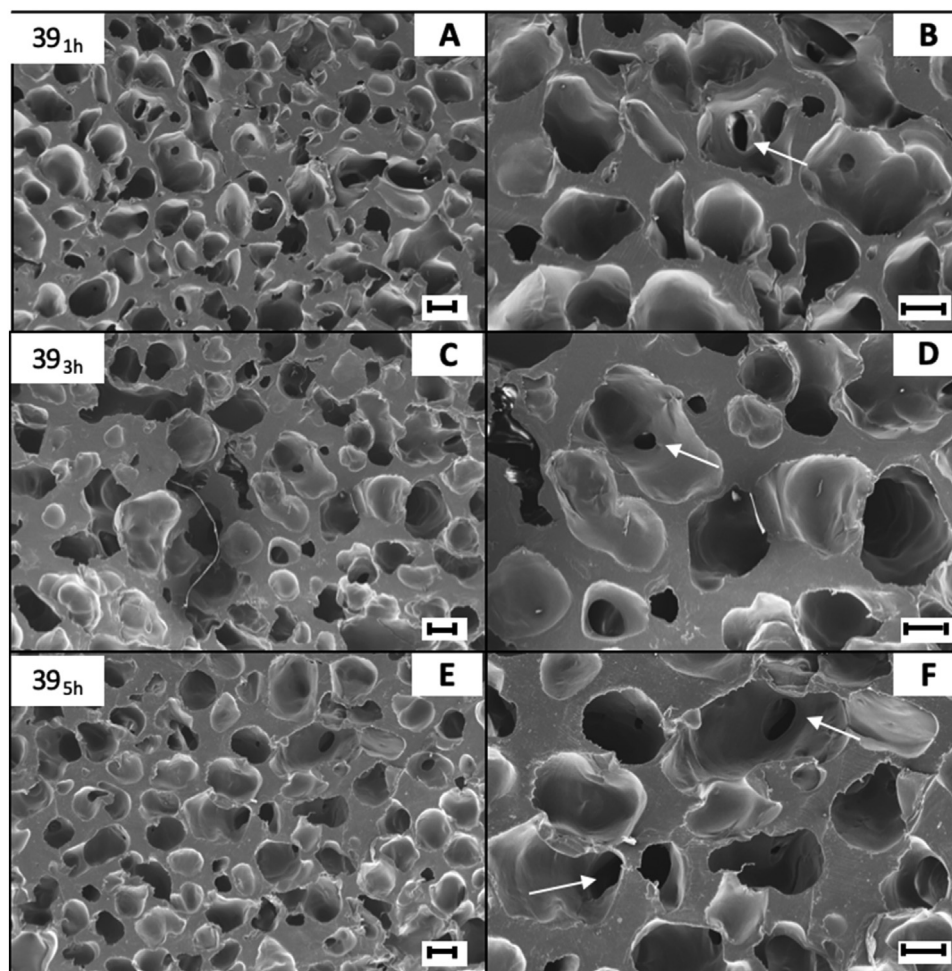
Fig. 3. SEM images of coronal cross-sections of the foamed PCL scaffolds processed at increasing soaking times: (A,B)1 h, (C,D) 3 h and (E,F) 5 h. Interconnected pores were obtained in all cases (white arrows in B,D,F). Scale bar: 200 μm.

values in the literature [54,55] are in fair agreement with this work, in spite of the differences in the molecular weight and crystallinity of the used PCL and in working pressures. It is reported that CO_2 dissolves to a higher extent in the amorphous regions of polymers and in polymers of lower molecular weights [56,57]. Finally, CO_2 solubility usually increases at higher pressures [17,54,58]. According to these results, the soaking times selected for further foaming trials were set at 1, 3 and 5 h to evaluate morphological differences depending on the increased amount of CO_2 dissolved in the PCL (0.238, 0.261 and 0.270 g CO_2/g PCL, respectively)

3.2. Sc-foaming process development and morphological characterization of the scaffolds

Cylindrical and highly porous PCL scaffolds (ε = 68–72 %) were obtained through sc-foaming, matching the human trabecular bone porosity values [59,60]. A dome-like top ending was observed for scaffolds processed with soaking times above 1 h in contact with the CO_2 at the foaming pressure (Figure S1). All specimens presented a non-porous skin of 100−140 μm thickness due to the rapid CO_2 diffusion upon depressurization from the surface of the PCL matrix [61]. Longer soaking times favored the polymeric expansion upon depressurization, slightly decreasing the bulk density values (ρ_{bulk}) of the manufactured scaffolds (Table 1).

The morphological analysis of the scaffolds from SEM microscopy images unveiled smooth surfaces with subtle differences among them regarding the pore geometries and densities (Fig. 3). 39$_{1h}$ scaffolds presented the less homogenous pore morphologies with small pores (<100 μm) combined with larger ones (Fig. 3A and B). Enhanced cell adhesion, migration, proliferation and differentiation are reported for polymeric scaffolds with a porous population in the 20–50 μm range [62,63]. Longer ST (5 h) favored the homogeneity and sphericity of the pores (39$_{5h}$ scaffolds in Fig. 3E and F). Qualitatively, scaffolds processed during 3 h pre-

Table 2
Pore throat and interconnectivities of PCL scaffolds processed by sc-foaming obtained from MIP and μ-CT data analysis.

Scaffold	MIP			μ-CT		
	MIP-mean pore throat diameter (μm)	Interconnectivity (%)	Tortuosity	μ-CT-mean pore throat diameter (μm)	Connected porosity (%)	Tortuosity
39_{1h}	35.26	71.17	1.5	242.3 ± 271.5	88.3	1.4
39_{3h}	36.86	79.00	1.2	285.8 ± 198.4	99.2	1.5
39_{5h}	35.63	77.83	1.3	148.9 ± 89.87	99.8	1.6

sented more void spaces along the analyzed area (39_{3h} scaffolds in Fig. 3C,D) than 39_{5h} scaffolds. All scaffolds had interconnected pores as highlighted by the presence of inner pores within the large pore cavities (white arrows in Fig. 3B, D and F).

Pore interconnectivity strongly influences the performance of the scaffolds since low levels can hamper the cell colonization phenomena and the diffusion of nutrients and removal of waste products from the cells [1,4]. The pore interconnectivity level of scaffolds obtained by sc-foaming can be modulated by modifications on the depressurization rate [18,64]. MIP technique allowed the study of open pore populations in the $0.01-180$ μm range to characterize the mesopores and the small macropore populations as well as degree of pore interconnection. The open porosity obtained by MIP (ε_{MIP}) of the foamed scaffold represented values in the 13–30 % range, clearly diverging from the overall porosity values (Table 1). This divergence in values can be attributed to the presence of pores either larger than 180 μm or closed. Namely, the lowest overall porosity was obtained for the 39_{3h} scaffold. The mean pore size calculated from MIP measurements unveiled that scaffolds processed at longer ST presented larger pores increasing up to 6 % for 39_{5h} scaffold (Table 1). The pore throat diameters were virtually identical, although differences in the degree of pore connection (interconnectivity) were obtained, mainly related to the different tortuosity of the scaffolds (Table 2). Overall, the manufactured scaffolds present good pore interconnectivity (above 70 %) for regenerative medicine purposes, regardless of the working parameters.
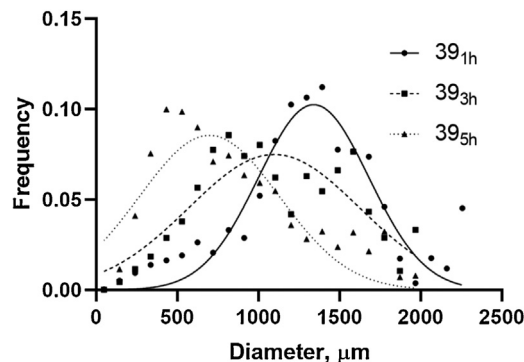
Fig. 4. Pore size distribution of the foamed PCL scaffolds processed at different soaking times (ST = 1, 3 and 5 h) obtained from 2D-image processing from micro X-ray computed tomography data. Longer ST resulted in lower mean pore diameters.

3.3. μ-CT imaging of PCL scaffolds obtained by sc-foaming using different soaking times

The presence of numerous pores with diameters larger than 200 μm (as observed by SEM) encouraged the use of μ-CT in order to effectively assess the effect of CO_2 soaking time on the resulting morphologies. Porosity values determined from μ-CT images ($\varepsilon_{\mu-CT}$) were in the 67–68 % range, being close to the overall poros-
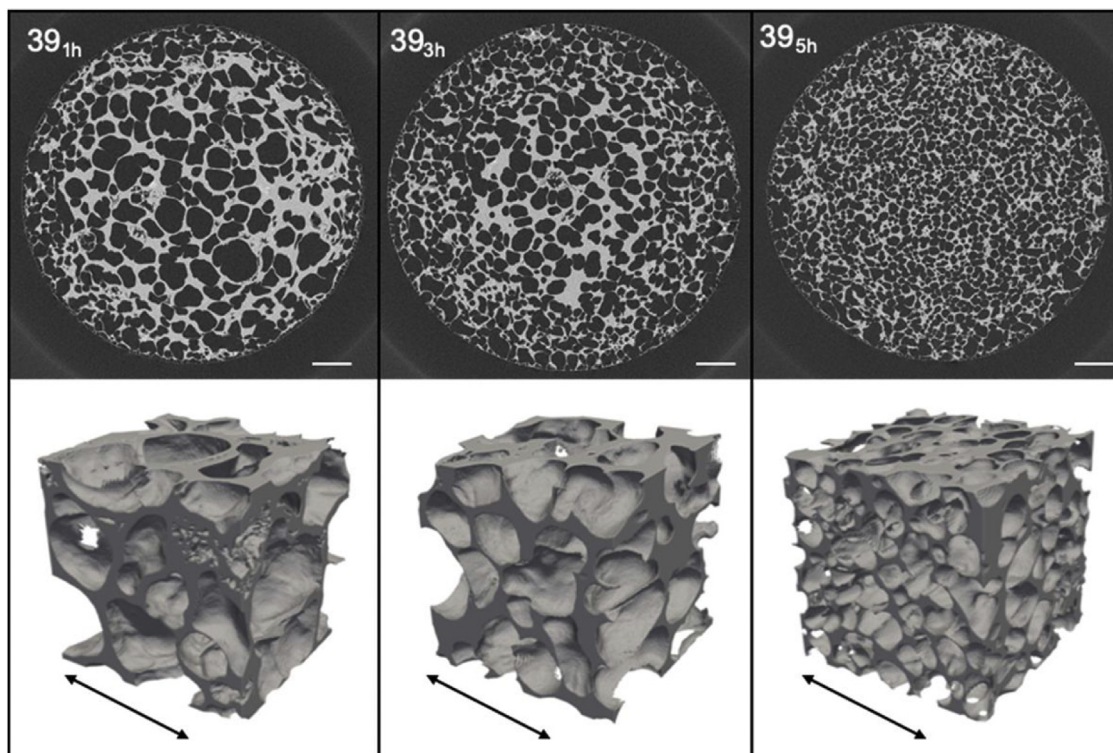
Fig. 5. 2D horizontal slices (top) of the foamed PCL scaffolds processed after increasing soaking times (from left to right, ST = 1, 3 and 5 h) with their corresponding 3D reconstructions (bottom) obtained from micro X-ray computed tomography data. Scale bars: 2 mm (top); arrow length: 2 mm (bottom).
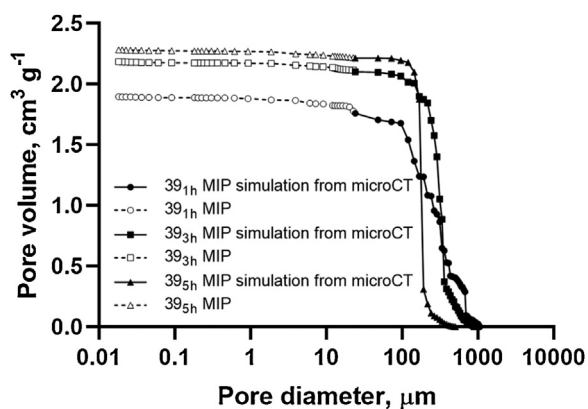
Fig. 6. Cumulative pore volume distribution of PCL scaffolds processed at 39 °C and 140 bar with different ST values. Distributions were obtained by combination obtained from MIP experimental data and from MIP simulated data from μ-CT, with a cut-off at a diameter of 25 μm.

ity values calculated from Eq. (1) (Table 1). Although all scaffolds had similar porosity values, remarkable differences in their morphology were observed in the 2D μ-CT images as a function of the processing time (ST). An increase in the number of pores and a reduction of the pore size was recorded as the ST increased (Figs. 4 and 5). An overestimation of the mean pore size was obtained from the analysis of the 2D axial plane sections when compared to the bulk structure, since the foams present elongated pores (Table 1). On the other hand, the total specific pore volume of the scaffolds calculated from μ-CT data underestimated in 5–10 % the values obtained from MIP analysis, since the volume contribution of small macropores and mesopores cannot be considered when μ-CT is used due to resolution limitations (Fig. 6).

The architecture of each scaffold was further analyzed from the data of the 3D-model obtained from the library of 2D slices (Fig. 7). Longer soaking times led to a reduction in the mean pore sizes of the scaffolds and narrower pore size distribution. Particularly, 39_{5h} scaffolds presented a narrow pore size distribution with values falling in the ideal size range $(1-500 \mu m)$ for bone tissue engineering [65,66]. These results are in line with previous studies with neat PCL scaffolds showing a remarkable reduction of the pore size with the increase of the soaking time [18]. Conversely, other study [67] reported the opposite effect during the supercritical foaming of pure PCL scaffolds, where the lowest pore diameters $(11.75 \mu m)$ were obtained after ST = 1 h. Overall, the reduction of the pore size of the foamed scaffolds obtained in this work follows the classical nucleation-growth theory of pore formation [68,69]. At longer processing times, higher initial amounts of CO_2 are dissolved within the polymer (Fig. 2) lowering the interfacial tension of the PCL-CO_2 system. This reduction in interfacial tension facilitates the formation of more nucleation sites since the initial critical nucleation radius is reduced [70–72]. Then, upon depressurization, scaffolds of higher cell densities with smaller pores are typically obtained when processed at longer soaking times [18,71]. The reduction in pore size is a consequence of the spatial limitation to the growth of pores from these nucleation sites due to their high abundance. Moreover, longer soaking times allow for a more efficient CO_2 distribution along the polymeric matrix resulting in more uniform and narrower pore distributions [32]. Both effects are easily appreciated in Fig. 7 as the soaking time increased.

Scaffolds allowing the infiltration of cells within their porous structures and the transport of nutrients, metabolites and wastes through them are needed to match the demands of the bone regeneration process. These properties are strongly dependent on the morphological properties of the scaffolds regarding pore and throat size distribution as well as the pore interconnectivity. The

Table 3
In silico predicted values of water permeability and MSCs infiltration on sc-foamed PCL scaffolds.

Scaffold	Water permeability (m^2)	Cell infiltration (%)
39_{1h}	$1.37 \cdot 10^{-13}$	66
39_{3h}	$1.42 \cdot 10^{-13}$	77
39_{5h}	$1.84 \cdot 10^{-12}$	93

degree of connected porosity in the scaffolds and how the pores are interlinked were characterized by the pore throat analysis. These features are of utmost importance since inhibition effects on the tissue differentiation process were reported for porous implants of narrow pore throats [73]. The increase in the soaking time resulted in scaffolds showing a reduction on the mean throat diameters and narrower throat size distribution, following a similar trend to the pore sizes discussed above (Table 2 and Fig. 7). Furthermore, the decrease in the mean throat size resulted in an increase on the tortuosity values, although the degree of connected void fraction was almost 100 % for the longer soaking time tested (39_{5h} scaffold).

### 3.4. *In silico* modelling of water permeability and human MSCs infiltration

The microstructure of scaffolds plays a critical role in cell infiltration and distribution of biological fluids [74]. Despite the intrinsic limitations of MIP technique previously presented, it widely covers pore populations below 10 μm, unreachable by both μ-CT (with the selected acquisition parameters) and MIP *in silico* simulation based on μ-CT data (Fig. 6). Therefore, the simulation of the permeability and cell infiltration values of the obtained scaffolds was based on experimental MIP data.

Water permeability values of 39_{1h} and 39_{3h} scaffolds (Table 3) were of the same order of magnitude to those reported *in silico* for PCL scaffolds obtained by sc-foaming at 37 °C and the same pressure [75], and *in vitro* for low molecular weight-PLGA scaffolds (*ca.* 10^{-13} m^2) with similar porous structures [76]. The increase of soaking time augmented water permeability and 39_{5h} scaffolds displayed one order of magnitude larger values. Overall, the obtained *in silico* permeability values for the manufactured scaffolds were close to the lowest experimental data reported for cancellous bone (10^{-12} to 10^{-8} m^2) [77,78]. Nevertheless, scaffold permeability was based on a water flow in a single axis direction and differences are expected as the structures have anisotropic properties. For instance, not only directional but also spatial differences in permeability calculations were reported for human [79], porcine [80] and bovine [81] cancellous bone. Despite the abovementioned limitations of the *in silico* model, permeability values were of the same order of magnitude to those reported for natural bone by experimental perfusion methods [78].

The cell infiltration capacity in the PCL scaffold was evaluated through the spread capacity of particles with defined sizes (corresponding to human MSCs dimensions). 39_{5h} scaffold had cell infiltration values over 90 %, suggesting that this structure may have full accessibility for cells once implanted, allowing a homogeneous tissue ingrowth instead of restricting it to the outer surface of the scaffold. Lower cell infiltration values were obtained for 39_{1h} and 39_{3h} scaffolds. Results should be sparingly considered since the model in this work was based on individual and non-interacting particles. For instance, the formation of undesired cell aggregates or clusters during the cell seeding period may occur, being a source of variability in the *in vitro* determination of cell infiltration [82].

Overall, 39_{5h} scaffold is the most promising candidate regarding its further biological performance as synthetic bone grafts in terms of water permeability and cell infiltration capacity.
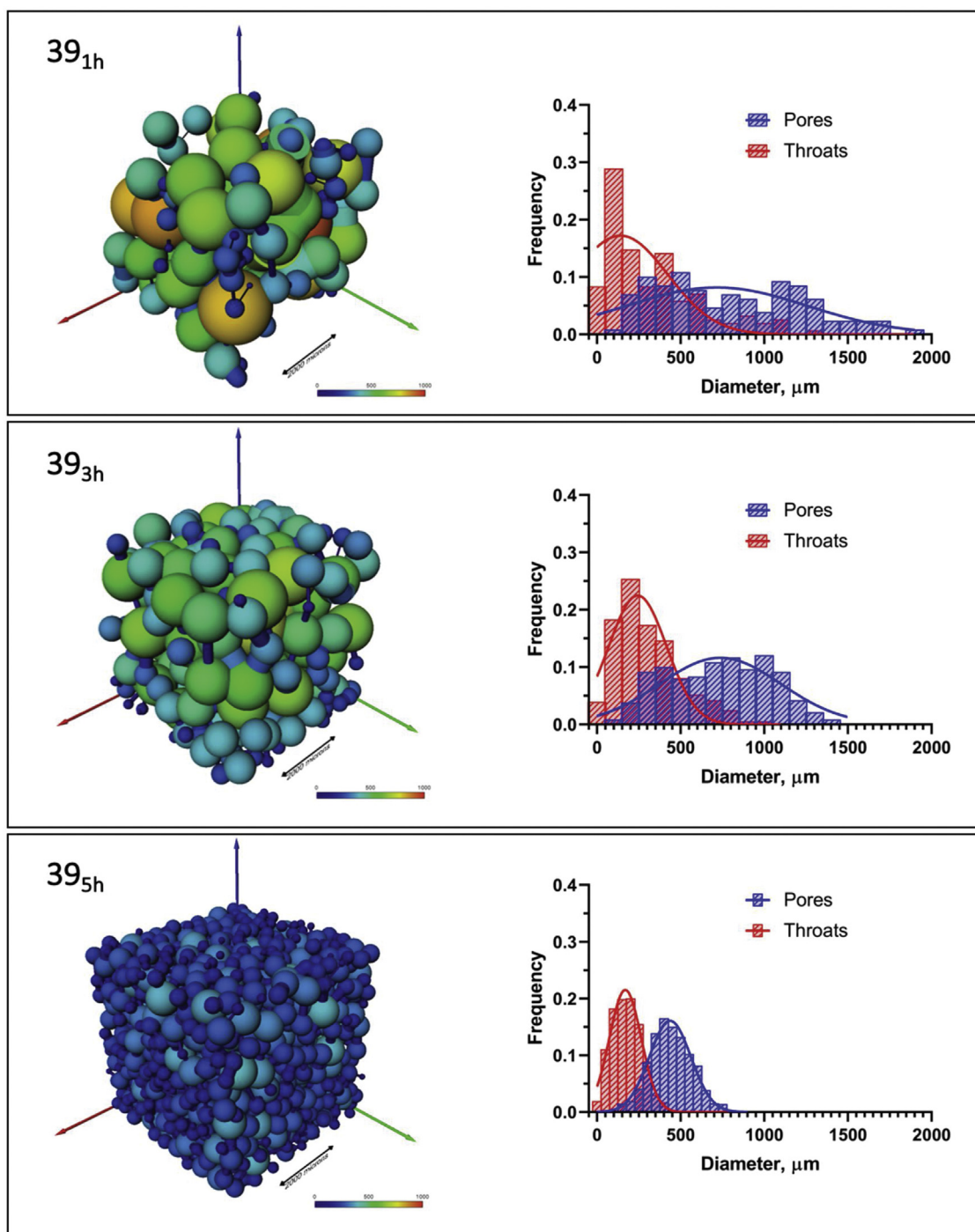
Fig. 7. 3D network models (left) of balls (pores) and struts (pore throats) representing the void fraction of the sc-foamed PCL scaffolds under increasing soaking times (from top to bottom, ST = 1, 3 and 5 h), coupled with their corresponding size distributions plots (right). Prolonged ST resulted in scaffolds with lower mean pore and throat sizes and with narrower size distributions.

3.5. Mechanical properties

Mechanical performance of scaffolds directly correlates to the structural modifications induced by the variation of processing conditions. During the foaming process, the CO_2 was vented in a single direction and the polymer expansion was forced to occur preferentially in the vertical axis, obtaining PCL foams with elongated pores mimicking the natural bone anisotropy (Fig. 3) [83]. Scaffolds presented an elastic deformation of *ca.* 25 % (Figure S2) and the obtained Young's moduli were in the 5−8 MPa range (Table 4), being in the reported range for

Table 4
Mechanical characterization of the sc-foamed PCL scaffolds. Mean values and standard deviation (n = 3). Results were statistically identical (1-way ANOVA; p < 0.05).

Scaffold	Elastic deformation (%)	Young's Modulus (MPa)
39_{1h}	23.8 ± 0.5	6.9 ± 0.1
39_{3h}	23.9 ± 1.8	6.3 ± 0.9
39_{5h}	25.4 ± 2.1	6.8 ± 0.5

human cancellous bone (1−900 MPa) [59]. Despite the morphological differences and the increase in cell density, the increase of the soaking time had no significant impact on the mechanical

behavior of the scaffolds when subjected to uniaxial compression stresses.

4. Conclusions

The architecture of porous PCL scaffolds produced by supercritical CO_2 foaming can be tailored by modifications of the processing conditions to provide highly adaptable scaffolds. From the μ-CT analysis, realistic scaffold reconstructions were obtained, being particularly useful to analyze the effect of the processing conditions on the resulting morphologies. Longer soaking times permit more CO_2 to be dissolved in the polymeric matrix, leading to higher density of pores with lower sizes. In addition, more homogeneous scaffolds and higher degree of pore interconnection were obtained with longer soaking times. On the other hand, MIP allowed the characterization of the meso- and low macro-pore population and of the degree of pore interconnection. This is of particular interest since the graft performance after implantation can be highly affected by these pore populations. In this sense and based on MIP measurements, the *in silico* modelling of cell infiltration capacity and water permeability of the obtained scaffolds constituted a potential screening tool for further *in vitro/in vivo* biological tests. The combination of complementary characterization techniques (μ-CT and MIP) coupled to the modelling of the generated data, offers not only broader and more realistic information regarding the manufactured scaffolds but also regarding their potential use as synthetic bone grafts. Overall, the herein presented supercritical CO_2 foaming process allows the manufacture of PCL scaffolds meeting the structural and mechanical requirements for bone tissue regeneration purposes. This work represents a step forward towards the knowledge on process-structure-functionality relationships in synthetic bone grafts for the definition of standard operating procedures in the manufacturing of poly(ε-caprolactone) scaffolds by supercritical CO_2 foaming.

Declaration of Competing Interest

Authors declare no conflict of interest.

Acknowledgments

Appendix A. Supplementary data

Supplementary material related to this article can be found, in the online version, at doi:https://doi.org/10.1016/j.supflu.2020.105012.

References

[1] C.A. García-González, A. Concheiro, C. Alvarez-Lorenzo, Processing of materials for regenerative medicine using supercritical fluid technology, Bioconjug. Chem. 26 (2015) 1159–1171, http://dx.doi.org/10.1021/bc5005922.

[2] S. Pina, V.P. Ribeiro, C.F. Marques, F.R. Maia, T.H. Silva, R.L. Reis, J.M. Oliveira, Scaffolding strategies for tissue engineering and regenerative medicine applications, Materials 12 (2019) 1824, http://dx.doi.org/10.3390/ma12111824.

[3] A. Eltom, G. Zhong, A. Muhammad, Scaffold techniques and designs in tissue engineering functions and purposes: a review, Adv. Mater. Sci. Eng. Int. J. 2019 (2019) 1–13, http://dx.doi.org/10.1155/2019/3429527.

[4] V. Santos-Rosales, A. Iglesias-Mejuto, C.A. García-González, Solvent-free approaches for the processing of scaffolds in regenerative medicine, Polymers 12 (2020) 533, http://dx.doi.org/10.3390/polym12030533.

[5] M.H. Sheridan, L.D. Shea, M.C. Peters, D.J. Mooney, Bioabsorbable polymer scaffolds for tissue engineering capable of sustained growth factor delivery, J. Control. Release 64 (2000) 91–102, http://dx.doi.org/10.1016/S0168-3659(99)00138-8.

[6] X.B. Yang, M.J. Whitaker, W. Sebald, N. Clarke, S.M. Howdle, K.M. Shakesheff, R.O.C. Oreffo, Human osteoprogenitor bone formation using encapsulated bone morphogenetic protein 2 in porous polymer scaffolds, Tissue Eng. 10 (2004) 1037–1045, http://dx.doi.org/10.1089/ten.2004.10.1037.

[7] L. Diaz-Gomez, F. Yang, J.A. Jansen, A. Concheiro, C. Alvarez-Lorenzo, C.A. García-González, Low viscosity-PLGA scaffolds by compressed CO_2 foaming for growth factor delivery, RSC Adv. 6 (2016) 70510–70519, http://dx.doi.org/10.1039/C6RA09369H.

[8] L. Goimil, V. Santos-Rosales, A. Delgado, C. Évora, R. Reyes, A.A. Lozano-Pérez, S.D. Aznar-Cervantes, J.L. Cenis, J.L. Gómez-Amoza, A. Concheiro, C. Alvarez-Lorenzo, C.A. García-González, scCO2-foamed silk fibroin aerogel/poly(ε-caprolactone) scaffolds containing dexamethasone for bone regeneration, J. CO2 Util. 31 (2019) 51–64, http://dx.doi.org/10.1016/j.jcou.2019.02.016.

[9] L.I. Cabezas, V. Fernández, R. Mazarro, I. Gracia, A. de Lucas, J.F. Rodríguez, Production of biodegradable porous scaffolds impregnated with indomethacin in supercritical CO2, J. Supercrit. Fluids 63 (2012) 155–160, http://dx.doi.org/10.1016/j.supflu.2011.12.002.

[10] R. Boia, P.A.N. Dias, J.M. Martins, C. Galindo-Romero, I.D. Aires, M. Vidal-Sanz, M. Agudo-Barriuso, H.C. de Sousa, A.F. Ambrósio, M.E.M. Braga, A.R. Santiago, Porous poly(ε-caprolactone) implants: A novel strategy for efficient intraocular drug delivery, J. Control. Release 316 (2019) 331–348, http://dx.doi.org/10.1016/j.jconrel.2019.09.023.

[11] C.A. García-González, J. Barros, A. Rey-Rico, P. Redondo, J.L. Gómez-Amoza, A. Concheiro, C. Alvarez-Lorenzo, F.J. Monteiro, Antimicrobial Properties and Osteogenicity of Vancomycin-Loaded Synthetic Scaffolds Obtained by Supercritical Foaming, ACS Appl. Mater. Interfaces 10 (2018) 3349–3360, http://dx.doi.org/10.1021/acsami.7b17375.

[12] Y.X.J. Ong, L.Y. Lee, P. Davoodi, C.-H. Wang, Production of drug-releasing biodegradable microporous scaffold using a two-step micro-encapsulation/supercritical foaming process, J. Supercrit. Fluids 133 (2018) 263–269, http://dx.doi.org/10.1016/j.supflu.2017.10.018.

[13] K. Gong, M. Braden, M.P. Patel, I.U. Rehman, Z. Zhang, J.A. Darr, Controlled release of chlorhexidine diacetate from a porous methacrylate system: supercritical fluid assisted foaming and impregnation, J. Pharm. Sci. 96 (2007) 2048–2056, http://dx.doi.org/10.1002/jps.20850.

[14] Y.-M. Corre, A. Maazouz, J. Duchet, J. Reignier, Batch foaming of chain extended PLA with supercritical CO2: influence of the rheological properties and the process parameters on the cellular structure, J. Supercrit. Fluids 58 (2011) 177–188, http://dx.doi.org/10.1016/j.supflu.2011.03.006.

[15] X.H. Zhu, L.Y. Lee, J.S.H. Jackson, Y.W. Tong, C.-H. Wang, Characterization of porous poly(D,L-lactic-co-glycolic acid) sponges fabricated by supercritical CO2 gas-foaming method as a scaffold for three-dimensional growth of Hep3B cells, Biotechnol. Bioeng. 100 (2008) 998–1009, http://dx.doi.org/10.1002/bit.21824.

[16] S. Milovanovic, D. Markovic, A. Mrakovic, R. Kuska, I. Zizovic, S. Frerich, J. Ivanovic, Supercritical CO2 - assisted production of PLA and PLGA foams for controlled thymol release, Mater. Sci. Eng. C 99 (2019) 394–404, http://dx.doi.org/10.1016/j.msec.2019.01.106.

[17] M.A. Fanovich, P. Jaeger, Sorption and diffusion of compressed carbon dioxide in polycaprolactone for the development of porous scaffolds, Mater. Sci. Eng. C 32 (2012) 961–968, http://dx.doi.org/10.1016/j.msec.2012.02.021.

[18] C.-X. Chen, Q.-Q. Liu, X. Xin, Y.-X. Guan, S.-J. Yao, Pore formation of poly(ε-caprolactone) scaffolds with melting point reduction in supercritical CO2 foaming, J. Supercrit. Fluids 117 (2016) 279–288, http://dx.doi.org/10.1016/j.supflu.2016.07.006.

[19] S.H. Kim, Y. Jung, S.H. Kim, A biocompatible tissue scaffold produced by supercritical fluid processing for cartilage tissue engineering, Tissue Eng. Part C Methods 19 (2013) 181–188, http://dx.doi.org/10.1089/ten.tec.2012.0170.

[20] E. Di Maio, E. Kiran, Foaming of polymers with supercritical fluids and perspectives on the current knowledge gaps and challenges, J. Supercrit. Fluids 134 (2018) 157–166, http://dx.doi.org/10.1016/j.supflu.2017.11.013.

[21] C.-X. Chen, H.-H. Peng, Y.-X. Guan, S.-J. Yao, Morphological study on the pore growth profile of poly(ε-caprolactone) bi-modal porous foams using a

modified supercritical CO2 foaming process, J. Supercrit. Fluids 143 (2019) 72–81, http://dx.doi.org/10.1016/j.supflu.2018.07.029.

[22] A. Salerno, C. Domingo, J. Saurina, PCL foamed scaffolds loaded with 5-fluorouracil anti-cancer drug prepared by an eco-friendly route, Mater. Sci. Eng. C 75 (2017) 1191–1197, http://dx.doi.org/10.1016/j.msec.2017.03.011.

[23] T. Kuang, F. Chen, L. Chang, Y. Zhao, D. Fu, X. Gong, X. Peng, Facile preparation of open-cellular porous poly (l-lactic acid) scaffold by supercritical carbon dioxide foaming for potential tissue engineering applications, Chem. Eng. J. 307 (2017) 1017–1025, http://dx.doi.org/10.1016/j.cej.2016.09.023.

[24] M. Zhao, X. Ding, J. Mi, H. Zhou, X. Wang, Role of high-density polyethylene in the crystallization behaviors, rheological property, and supercritical CO2 foaming of poly (lactic acid), Polym. Degrad. Stab. 146 (2017) 277–286, http://dx.doi.org/10.1016/j.polymdegradstab.2017.11.003.

[25] S.T. Ho, D.W. Hutmacher, A comparison of micro CT with other techniques used in the characterization of scaffolds, Biomaterials 27 (2006) 1362–1376, http://dx.doi.org/10.1016/j.biomaterials.2005.08.035.

[26] P.A. Webb, An Introduction to the Physical Characterization of Materials by Mercury Intrusion Porosimetry with Emphasis on Reduction and Presentation of Experimental Data, Micromeritics Instrument Corp, Norcross GA, USA, 2001.

[27] A. Gomez-Carracedo, R. Martinez-Pacheco, A. Concheiro, J.L. Gomez-Amoza, Modelling of porosity and waterfronts in cellulosic pellets for understanding drug release behavior, Int. J. Pharm. 388 (2010) 101–106, http://dx.doi.org/10.1016/j.ijpharm.2009.12.038.

[28] C.A. León y León, New perspectives in mercury porosimetry, Adv. Colloid Interface Sci. 76–77 (1998) 341–372, http://dx.doi.org/10.1016/S0001-8686(98)00052-9.

[29] H. Giesche, Mercury porosimetry: a general (Practical) overview, Part. Part. Syst. Charact. 23 (2006) 9–19, http://dx.doi.org/10.1002/ppsc.200601009.

[30] N.G. Kalatzis-Sousa, R. Spin-Neto, A. Wenzel, M. Tanomaru-Filho, G. Faria, Use of micro-computed tomography for the assessment of periapical lesions in small rodents: a systematic review, Int. Endod. J. 50 (2017) 352–366, http://dx.doi.org/10.1111/iej.12633.

[31] I.F. Cengiz, J.M. Oliveira, R.L. Reis, Micro-CT – a digital 3D microstructural voyage into scaffolds: a systematic review of the reported methods and results, Biomater. Res. 22 (2018), http://dx.doi.org/10.1186/s40824-018-0136-8.

[32] H. Tai, M. Mather, D. Howard, W. Wang, L. White, J. Crowe, S. Morgan, A. Chandra, D. Williams, S. Howdle, K. Shakesheff, Control of pore size and structure of tissue engineering scaffolds produced by supercritical fluid processing, Eur. Cell. Mater. 14 (2007) 64–77, http://dx.doi.org/10.22203/eCM.v014a07.

[33] R.M. Duarte, J. Correia-Pinto, R.L. Reis, A.R.C. Duarte, Subcritical carbon dioxide foaming of polycaprolactone for bone tissue regeneration, J. Supercrit. Fluids 140 (2018) 1–10, http://dx.doi.org/10.1016/j.supflu.2018.05.019.

[34] L.J. White, V. Hutter, H. Tai, S.M. Howdle, K.M. Shakesheff, The effect of processing variables on morphological and mechanical properties of supercritical CO2 foamed scaffolds for tissue engineering, Acta Biomater. 8 (2012) 61–71, http://dx.doi.org/10.1016/j.actbio.2011.07.032.

[35] E. Askari, I.F. Cengiz, J.L. Alves, B. Henriques, P. Flores, M.C. Fredel, R.L. Reis, J.M. Oliveira, F.S. Silva, J. Mesquita-Guimarães, Micro-CT based finite element modelling and experimental characterization of the compressive mechanical properties of 3-D zirconia scaffolds for bone tissue engineering, J. Mech. Behav. Biomed. Mater. 102 (2020), 103516, http://dx.doi.org/10.1016/j.jmbbm.2019.103516.

[36] M. Karimi, M. Heuchel, T. Weigel, M. Schossig, D. Hofmann, A. Lendlein, Formation and size distribution of pores in poly(ε-caprolactone) foams prepared by pressure quenching using supercritical CO2, J. Supercrit. Fluids 61 (2012) 175–190, http://dx.doi.org/10.1016/j.supflu.2011.09.022.

[37] L. Mathieu, T. Mueller, P. Bourban, D. Pioletti, R. Muller, J. Manson, Architecture and properties of anisotropic polymer composite scaffolds for bone tissue engineering, Biomaterials 27 (2006) 905–916, http://dx.doi.org/10.1016/j.biomaterials.2005.07.015.

[38] I.F. Cengiz, J.M. Oliveira, R.L. Reis, Micro-computed tomography characterization of tissue engineering scaffolds: effects of pixel size and rotation step, J. Mater. Sci. Mater. Med. 28 (2017), http://dx.doi.org/10.1007/s10856-017-5942-3.

[39] Z. Heydari, D. Mohebbi-Kalhori, M.S. Afarani, Engineered electrospun polycaprolactone (PCL)/octacalcium phosphate (OCP) scaffold for bone tissue engineering, Mater. Sci. Eng. C 81 (2017) 127–132, http://dx.doi.org/10.1016/j.msec.2017.07.041.

[40] S. Hassanajili, A. Karami-Pour, A. Oryan, T. Talaei-Khozani, Preparation and characterization of PLA/PCL/HA composite scaffolds using indirect 3D printing for bone tissue engineering, Mater. Sci. Eng. C 104 (2019), 109960, http://dx.doi.org/10.1016/j.msec.2019.109960.

[41] Y. Du, H. Liu, Q. Yang, S. Wang, J. Wang, J. Ma, I. Noh, A.G. Mikos, S. Zhang, Selective laser sintering scaffold with hierarchical architecture and gradient composition for osteochondral repair in rabbits, Biomaterials 137 (2017) 37–48, http://dx.doi.org/10.1016/j.biomaterials.2017.05.021.

[42] S.Y. Tong, Z. Wang, P.N. Lim, W. Wang, E.S. Thian, Uniformly-dispersed nanohydroxapatite-reinforced poly(ε-caprolactone) composite films for tendon tissue engineering application, Mater. Sci. Eng. C 70 (2017) 1149–1155, http://dx.doi.org/10.1016/j.msec.2016.03.051.

[43] S.J. Lee, H.-J. Kim, M. Heo, H.-R. Lee, E.-J. Choi, H. Kim, D. Lee, R.L. Reis, S.H. Do, I.K. Kwon, In vitro and in vivo assessments of an optimal polyblend composition of polycaprolactone/gelatin nanofibrous scaffolds for Achilles tendon tissue engineering, J. Ind. Eng. Chem. 76 (2019) 173–180, http://dx.doi.org/10.1016/j.jiec.2019.03.036.

[44] T. Fukunishi, C.A. Best, T. Sugiura, T. Shoji, T. Yi, B. Udelsman, D. Ohst, C.S. Ong, H. Zhang, T. Shinoka, C.K. Breuer, J. Johnson, N. Hibino, Tissue-engineered small diameter arterial vascular grafts from cell-free nanofiber PCL/Chitosan scaffolds in a sheep model, PLoS One 11 (2016), e0158555, http://dx.doi.org/10.1371/journal.pone.0158555.

[45] M.O. Aydogdu, J. Chou, E. Altun, N. Ekren, S. Cakmak, M. Eroglu, A.A. Osman, O. Kutlu, E.T. Oner, G. Avsar, F.N. Oktar, I. Yilmaz, O. Gunduz, Production of the biomimetic small diameter blood vessels for cardiovascular tissue engineering, Int. J. Polym. Mater. Polym. Biomater. 68 (2019) 243–255, http://dx.doi.org/10.1080/00914037.2018.1443930.

[46] L. Goimil, P. Jaeger, I. Ardao, J.L. Gómez-Amoza, A. Concheiro, C. Alvarez-Lorenzo, C.A. García-González, Preparation and stability of dexamethasone-loaded polymeric scaffolds for bone regeneration processed by compressed CO 2 foaming, J. CO2 Util. 24 (2018) 89–98, http://dx.doi.org/10.1016/j.jcou.2017.12.012.

[47] J. Ge, L. Guo, S. Wang, Y. Zhang, T. Cai, R.C.H. Zhao, Y. Wu, The size of mesenchymal stem cells is a significant cause of vascular obstructions and stroke, Stem Cell Rev. Rep. 10 (2014) 295–303, http://dx.doi.org/10.1007/s12015-013-9492-x.

[48] T.J. Bartosh, J.H. Ylostalo, A. Mohammadipoor, N. Bazhanov, K. Coble, K. Claypool, R.H. Lee, H. Choi, D.J. Prockop, Aggregation of human mesenchymal stromal cells (MSCs) into 3D spheroids enhances their antiinflammatory properties, Proc. Natl. Acad. Sci. U. S. A. 107 (2010) 13724–13729, http://dx.doi.org/10.1073/pnas.1008117107.

[49] A. Salerno, S. Diéguez, L. Diaz-Gomez, J.L. Gómez-Amoza, B. Magariños, Angel Concheiro, C. Domingo, C. Alvarez-Lorenzo, Synthetic scaffolds with full pore interconnectivity for bone regeneration prepared by supercritical foaming using advanced biofunctional plasticizers, Biofabrication 9 (2017), 035002.

[50] S.-Y. Chung, J.-S. Kim, D. Stephan, T.-S. Han, Overview of the use of micro-computed tomography (micro-CT) to investigate the relation between the material characteristics and properties of cement-based materials, Constr. Build. Mater. 229 (2019), 116843, http://dx.doi.org/10.1016/j.conbuildmat.2019.116843.

[51] B. Münch, L. Holzer, Contradicting geometrical concepts in pore size analysis attained with Electron microscopy and mercury intrusion, J. Am. Ceram. Soc. 91 (2008) 4059–4067, http://dx.doi.org/10.1111/j.1551-2916.2008.02736.x.

[52] J. Schindelin, I. Arganda-Carreras, E. Frise, V. Kaynig, M. Longair, T. Pietzsch, S. Preibisch, C. Rueden, S. Saalfeld, B. Schmid, J.-Y. Tinevez, D.J. White, V. Hartenstein, K. Eliceiri, P. Tomancak, A. Cardona, Fiji: an open-source platform for biological-image analysis, Nat. Methods 9 (2012) 676–682, http://dx.doi.org/10.1038/nmeth.2019.

[53] D.L. Tomasko, H. Li, D. Liu, X. Han, M.J. Wingert, L.J. Lee, K.W. Koelling, A review of CO_2 applications in the processing of polymers, Ind. Eng. Chem. Res. 42 (2003) 6431–6456, http://dx.doi.org/10.1021/ie030199z.

[54] J. Ivanovic, S. Knauer, A. Fanovich, S. Milovanovic, M. Stamenic, P. Jaeger, I. Zizovic, R. Eggers, Supercritical CO 2 sorption kinetics and thymol impregnation of PCL and PCL-HA, J. Supercrit. Fluids 107 (2016) 486–498, http://dx.doi.org/10.1016/j.supflu.2015.07.001.

[55] M.A. Fanovich, J. Ivanovic, I. Zizovic, D. Misic, P. Jaeger, Functionalization of polycaprolactone/hydroxyapatite scaffolds with Usnea lethariiformis extract by using supercritical CO2, Mater. Sci. Eng. C 58 (2016) 204–212, http://dx.doi.org/10.1016/j.msec.2015.08.024.

[56] E. Aionicesei, M. Škerget, Ž. Knez, Mathematical modelling of the solubility of supercritical CO2 in poly(l-lactide) and poly(d,l-lactide-co-glycolide), J. Supercrit. Fluids 50 (2009) 320–326, http://dx.doi.org/10.1016/j.supflu.2009.06.002.

[57] E. Markočič, M. Škerget, Ž. Knez, Solubility and diffusivity of CO2 in poly(l-lactide)–hydroxyapatite and poly(d,l-lactide-co-glycolide)–hydroxyapatite composite biomaterials, J. Supercrit. Fluids 55 (2011) 1046–1051, http://dx.doi.org/10.1016/j.supflu.2010.10.001.

[58] S. Lin, J. Yang, J. Yan, Y. Zhao, B. Yang, Sorption and diffusion of supercritical carbon dioxide in a biodegradable polymer, J. Macromol. Sci. Part B 49 (2010) 286–300, http://dx.doi.org/10.1080/01495930903352308.

[59] K.A. Athanasiou, C.-F. Zhu, D.R. Lanctot, C.M. Agrawal, X. Wang, Fundamentals of biomechanics in tissue engineering of bone, Tissue Eng. 6 (2000) 361–381, http://dx.doi.org/10.1089/107632700418083.

[60] K.A. Blackwood, N. Bock, T.R. Dargaville, M. Ann Woodruff, Scaffolds for growth factor delivery as applied to bone tissue engineering, Int. J. Polym. Sci. 2012 (2012) 1–25, http://dx.doi.org/10.1155/2012/174942.

[61] E. Markočič, M. Škerget, Ž. Knez, Effect of temperature and pressure on the behavior of Poly(ε-caprolactone) in the presence of supercritical carbon dioxide, Ind. Eng. Chem. Res. 52 (2013) 15594–15601, http://dx.doi.org/10.1021/ie402256a.

[62] A. Salerno, D. Guarnieri, M. Iannone, S. Zeppetelli, P.A. Netti, Effect of micro- and macroporosity of bone tissue three-dimensional-Poly(ε-Caprolactone) scaffold on human mesenchymal stem cells invasion, proliferation, and differentiation In Vitro, Tissue Eng. Part A 16 (2010) 2661–2673, http://dx.doi.org/10.1089/ten.tea.2009.0494.

[63] G. Akay, M.A. Birch, M.A. Bokhari, Microcellular polyHIPE polymer supports osteoblast growth and bone formation in vitro, Biomaterials 25 (2004) 3991–4000, http://dx.doi.org/10.1016/j.biomaterials.2003.10.086.

[64] L.J. White, V. Hutter, H. Tai, S.M. Howdle, K.M. Shakesheff, The effect of processing variables on morphological and mechanical properties of

supercritical CO2 foamed scaffolds for tissue engineering, Acta Biomater. 8 (2012) 61–71, http://dx.doi.org/10.1016/j.actbio.2011.07.032.

[65] S.J. Simske, R.A. Ayers, T.A. Bateman, Porous materials for bone engineering, Mater. Sci. Forum 250 (1997) 151–182, http://dx.doi.org/10.4028/www.scientific.net/MSF.250.151.

[66] F. Baino, S. Fiorilli, C. Vitale-Brovarone, Bioactive glass-based materials with hierarchical porosity for medical applications: review of recent advances, Acta Biomater. 42 (2016) 18–32, http://dx.doi.org/10.1016/j.actbio.2016.06.033.

[67] K. Kosowska, M. Henczka, The influence of supercritical foaming conditions on properties of polymer scaffolds for tissue engineering, Chem. Process Eng. 38 (2017) 535–541, http://dx.doi.org/10.1515/cpe-2017-0042.

[68] J.S. Colton, N.P. Suh, Nucleation of microcellular foam: theory and practice, Polym. Eng. Sci. 27 (1987) 500–503, http://dx.doi.org/10.1002/pen.760270704.

[69] V. Kumar, N.P. Suh, A process for making microcellular thermoplastic parts, Polym. Eng. Sci. 30 (1990) 1323–1329, http://dx.doi.org/10.1002/pen.760302010.

[70] S.K. Goel, E.J. Beckman, Generation of microcellular polymeric foams using supercritical carbon dioxide. I: effect of pressure and temperature on nucleation, Polym. Eng. Sci. 34 (1994) 1137–1147, http://dx.doi.org/10.1002/pen.760341407.

[71] S.K. Goel, E.J. Beckman, Generation of microcellular polymeric foams using supercritical carbon dioxide. II: cell growth and skin formation, Polym. Eng. Sci. 34 (1994) 1148–1156, http://dx.doi.org/10.1002/pen.760341408.

[72] V.I. Kalikmanov, Classical Nucleation Theory, in: Nucleation Theory, Springer Netherlands, Dordrecht, 2013, pp. 17–41, http://dx.doi.org/10.1007/978-90-481-3643-8_3.

[73] B. Otsuki, M. Takemoto, S. Fujibayashi, M. Neo, T. Kokubo, T. Nakamura, Pore throat size and connectivity determine bone and tissue ingrowth into porous implants: three-dimensional micro-CT based structural analyses of porous bioactive titanium implants, Biomaterials 27 (2006) 5892–5900, http://dx.doi.org/10.1016/j.biomaterials.2006.08.013.

[74] M. Mastrogiacomo, S. Scaglione, R. Martinetti, L. Dolcini, F. Beltrame, R. Cancedda, R. Quarto, Role of scaffold internal structure on in vivo bone formation in macroporous calcium phosphate bioceramics, Biomaterials 27 (2006) 3230–3237, http://dx.doi.org/10.1016/j.biomaterials.2006.01.031.

[75] L. Goimil, M.E.M. Braga, A.M.A. Dias, J.L. Gómez-Amoza, A. Concheiro, C. Alvarez-Lorenzo, H.C. de Sousa, C.A. García-González, Supercritical processing of starch aerogels and aerogel-loaded poly(ε-caprolactone) scaffolds for sustained release of ketoprofen for bone regeneration, J. CO2 Util. 18 (2017) 237–249, http://dx.doi.org/10.1016/j.jcou.2017.01.028.

[76] Y. Reinwald, R.K. Johal, A.M. Ghaemmaghami, F.R.A.J. Rose, S.M. Howdle, K.M. Shakesheff, Interconnectivity and permeability of supercritical fluid-foamed scaffolds and the effect of their structural properties on cell distribution, Polymer 55 (2014) 435–444, http://dx.doi.org/10.1016/j.polymer.2013.09.041.

[77] A. Syahrom, M.R. Abdul Kadir, J. Abdullah, A. Öchsner, Permeability studies of artificial and natural cancellous bone structures, Med. Eng. Phys. 35 (2013) 792–799, http://dx.doi.org/10.1016/j.medengphy.2012.08.011.

[78] A. Syahrom, M.R. Abdul Kadir, M.N. Harun, A. Öchsner, Permeability study of cancellous bone and its idealised structures, Med. Eng. Phys. 37 (2015) 77–86, http://dx.doi.org/10.1016/j.medengphy.2014.11.001.

[79] E.A. Nauman, K.E. Fong, T.M. Keaveny, Dependence of Intertrabecular Permeability on Flow Direction and Anatomic Site, Ann. Biomed. Eng. 27 (1999) 517–524, http://dx.doi.org/10.1114/1.195.

[80] M. Ito, S. Tupin, H. Anzai, A. Suzuki, M. Ohta, Experimental Analysis for the Anisotropic Flows in Cancellous Bone, in: Vol. 3 Biomed. Biotechnol. Eng., American Society of Mechanical Engineers, Tampa, Florida, USA, 2017, http://dx.doi.org/10.1115/IMECE2017-71346.

[81] S.S. Kohles, J.B. Roberts, M.L. Upton, C.G. Wilson, L.J. Bonassar, A.L. Schlichting, Direct perfusion measurements of cancellous bone anisotropic permeability, J. Biomech. 34 (2001) 1197–1202, http://dx.doi.org/10.1016/S0021-9290(01)00082-3.

[82] N. Ghavidel Mehr, X. Li, M.B. Ariganello, C.D. Hoemann, B.D. Favis, Poly(ε-caprolactone) scaffolds of highly controlled porosity and interconnectivity derived from co-continuous polymer blends: model bead and cell infiltration behavior, J. Mater. Sci. Mater. Med. 25 (2014) 2083–2093, http://dx.doi.org/10.1007/s10856-014-5256-7.

[83] L.M. Mathieu, M.-O. Montjovent, P.-E. Bourban, D.P. Pioletti, J.-A.E. Månson, Bioresorbable composites prepared by supercritical fluid foaming, J. Biomed. Mater. Res. A 75A (2005) 89–97, http://dx.doi.org/10.1002/jbm.a.30385.